Hole, M.J., Gibson, S.A., and Morris, M.C., 2023, Slab window–related magmatism as a probe for pyroxenite heterogeneities in the upper mantle: Geology, https://doi.org/10.1130/G50687.1

Slab window related magmatism as a probe for lithological variability in the upper mantle.

Malcolm J. Hole[1], Sally, A. Gibson[2], Matthew C. Morris[2].

1. Melt-PX parameters

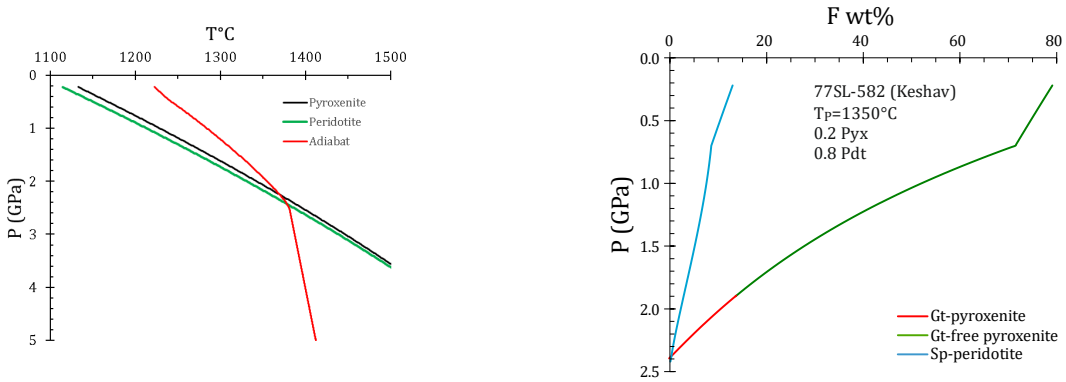

Fig. S.1. a) Pressure vs temperature and b) pressure vs % melt (F) diagram generated from Melt-PX for pyroxenite 77SL-582 (Keshav et al. 2004). The red and green curves in b) represent garnet-pyroxenite and garnet-free pyroxenite melting respectively. These curves are combined and used to calculate melt productivity GPa^{-1} in accumulated melt fraction models. Configuration is; T_P=1350°C; fraction of pyroxenite=0.2; mass fraction of clinopyroxene present in sub-solidus peridotite=0.24.

Our accumulated fractional melting model is based upon 1% increments of melting. We derive the pressure of melting for pyroxenite from a polynomial regression of the green line in Fig. S.1b over the pressure range of 2.33-0.70 GPa;

$$P=0.00019F^2+0.03623F+2.36759$$

Where F is % of melt.

Over the pressure range of interest (2.2-0.5 GPa), P-F is near linear for peridotite and we use the following equation;

$$P=-0.1861F+2.4267$$

2. Accumulated fractional melting model

a. Starting compositions.

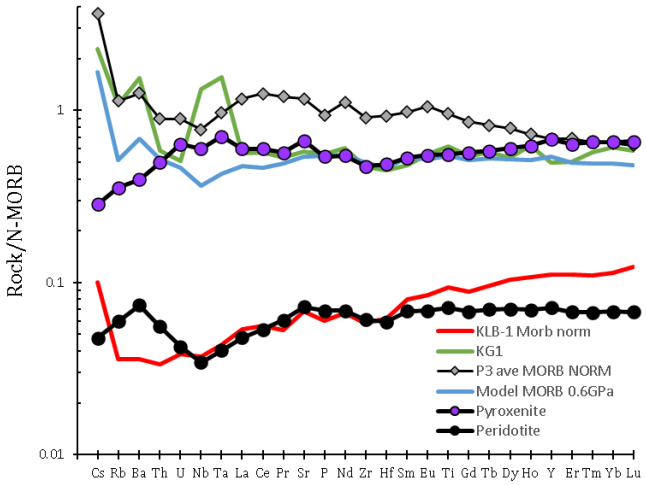

Fig. S.2. MORB-normalized multi-element plot for the model components used in this paper along with measured values for KLB-1, KG1 and Phoenix Ridge segment P3 N-MORB. The blue line is a calculated model peridotite melt at a final melting pressure of ~0.6 GPa. Normalisation factors are from Sun & McDonough (1989)

MORB mantle-normalized abundances of trace elements in the starting compositions are shown in Fig. S.2 and listed in Table S.1. The pyroxenite compositions is based on KG1 (Lambart, 2017) but lacks the large positive Nb, Ta anomaly, because this is not a feature of most ocean ridge basalts. The peridotite composition is based on KLB-1 (Lambart, 2017) but is slightly less depleted reflecting the composition of Phoenix Ridge N-MORB (grey diamonds in Fig. S.2). Calculated accumulated fractional melts of peridotite at 0.6 GPa are a good match to the pattern of Phoenix Ridge MORB.

b. Accumulated fractional melting.

Standard equations for mantle melting (Shaw, 1970) have been applied to calculate the concentrations of trace elements

For the concentration of a given element in the liquid (C_l); $$\frac{C_L}{C_0} = \frac{1}{D_0}\left(1 - {}^{PF}/_{D_0}\right)^{\left(\frac{1}{P-1}\right)}$$

And for the concentration of a given element in the solid (C_s); $$\frac{C_S}{C_0} = \frac{1}{(1-F)}\left(1 - {}^{PF}/_{D_0}\right)^{\left(\frac{1}{P}\right)}$$

Where D_o is the bulk partition coefficient, F is the melt fraction and P is the melting proportion

c. Partition coefficients

Partition coefficients are given in Tables S.1 & S.2 along with mineral modes used in the calculations. Partition coefficients for melting of MORB are those of McKenzie and O'Nions (1991), with additional data for transition elements from LeRoux *et al*. (2015). For pyroxenite we use data from Petermann *et al*. (2004) and LeRoux *et al*. (2015). While the values from Petermann *et al.* (2004) are for silica-deficient pyroxenite i.e. a MORB eclogite, we assume that for the elements shown in Fig. S.1 these are applicable. However, we are guarded in applying the very high D_{Ni} and D_{Cr} of Pertermann et al. (2004) to a silica-deficient pyroxenite. Fig. S.3 summarizes the bulk partition coefficients used in our model.

As we are mostly interested in the composition of small melt fractions, we have assumed the melting mode does not vary during melting. This is an oversimplification but for melting garnet pyroxenite it is the pressure at which garnet is no longer stable on the solidus that is more critical to the model than changing mode for garnet-present melting.

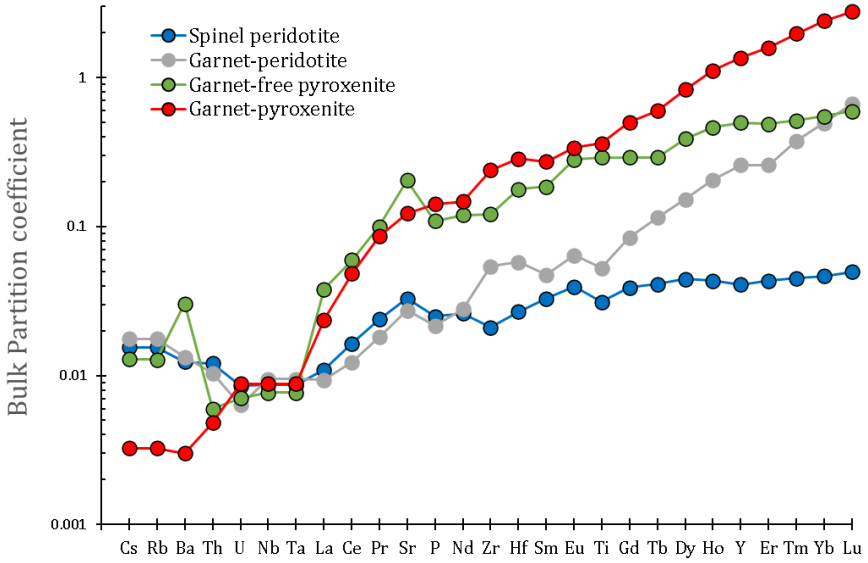

Fig. S.3 Log-plot of bulk partition coefficients used in the model. The data for garnet peridotite is for reference and is not utilized in the current model. Note that

bulk partition coefficients are generally much higher for MORB-like eclogite when compared to garnet peridotite (Pertermann *et al.* 2004) except for elements more incompatible than La.

d. First-formed melts of peridotite and pyroxenite melting in terms of 10^4Zn/Fe and 100Mn/Fe

For calculating the first formed melt on the 10^4Zn/Fe and 100Mn/Fe diagram at T_P=1350°C, we use a model MORB primary magma from the Siqueiros Fracture Zone from Herzberg & Asimow (2015) which contains 11.56 wt.% MgO and 8.17 wt.% FeO_T and represents ~9% melt. For smaller melt fractions, we assume that the melting trajectory is coincident with the olivine liquidus and adjust FeO_T and MgO accordingly. From the MgO and FeO_T of the melt we calculate the Fo content of equilibrium olivine and from that value the cation proportion of Fe and Mg in olivine and hence the FeO content of olivine. We assume FeO/FeO_T=0.88 (Herzberg & Asimow, 2015) equivalent to QFM-1. To obtain k_DMn we calculate $D_{\underline{MgO}}$ from the model magma and its equilibrium olivine and use the Herzberg & O'Hara (2002) expression:

$$k_D\text{Mn}=0.118D_{\text{MgO}}+0.214$$

For the first formed peridotite melts on the same diagram at 1500°C and 1550°C we use the following:

T_P1500°C; Hawaiian post-shield magma 0622-6. F=2.4% and 17.6 wt.% MgO, 10.7 wt.% FeO_T

T_P 1550°C; Disko Island picrite 362077. F=7.8% and 19.8 wt.% MgO, 11.3 wt.% FeO_T

Both model primary magmas are from Hole & Millet (2016).

For the T_P=1350°C melting trajectory for pyroxenite we use the parental magma to Seal Nunataks lava R.3717.1 (14.1 wt.% MgO; 10.9 wt.% FeO_T) and assume it was formed by ~10% melting at 1.9 GPa.

3. Relationship between pyroxenite bulk composition, P_i^{Pyx} and P_i^{Pdt}

Lambart et al. (2016) express pyroxenite compositions as;

$$(1\text{-Mg\#}) + 10(Na + K)\text{-}Ca + Al$$

Where; Mg# is the molar ratio MgO/(MgO + FeO) and Na, K, Ca, and Al are the mole fractions of Na_2O, K_2O, CaO, and Al_2O_3.

Figure S.4 shows the relationship between alkalinity index and pressure and extent of melting for silica-enriched and silica-depleted pyroxenite. In general, silica-enriched pyroxenite will melt at a higher pressure than silica-depleted pyroxenite for a given T_P (Fig. S.4a), but this is critically dependent on the non CMAS components i.e. alkalis and Ti (Lambart et al., 2013). This can be translated into the extent of melting of pyroxenite before peridotite joins the melting assemblage ($F@P_i^{Pdt}$; Fig. S.4b). For most silica-depleted pyroxenite at T_P =1350°C <13% melting will occur before peridotite begins to melt, whereas for most silica-enriched pyroxenite, F is >26%. Therefore, to enable mixing between small fraction melts of peridotite and small fraction melts of pyroxenite, $F@Pi^{Pdt}$ needs to be minimal. Pyroxenite 77SL-582 as used in this study (red dot in Fig. S.4) falls into that category.

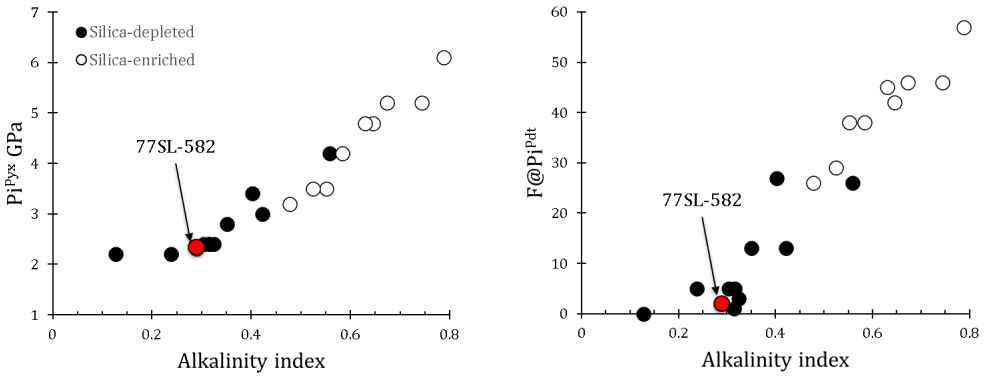

Fig S.4 a) Initial pressure of melting at T_P=1350°C *versus* alkalinity index of pyroxenite. Black dots are silica-depleted and white dots silica-enriched pyroxenites. b) Extent of melting of pyroxenite (F, wt.%) at the point at which peridotite joins the melting assemblage ($F@P_i^{Pdt}$) at T_P=1350°C *versus* alkalinity index. The red dot is for 77SL-582. The data point on the x-axis with alkalinity index ~0.13 is an olivine pyroxenite (OlCpx1; Lambart *et al.,* 2016).

4. Calculation of parental pyroxenite magma compositions.

Full details of the process are given by Herzberg (2011) and Hole (2021). Firstly, it is necessary to determine whether lava compositions are consistent with the crystallization of olivine alone. This can be done using major element compositions and with petrographic observation. We restrict the parental magma calculations to samples that have only olivine as a phenocryst phase and show no evidence of plagioclase fractionation in terms of MgO-CaO-Al_2O_3 variations. Selected samples are then recalculated as mole% and the projection coordinates given by Herzberg (2011) are calculated. Data are then plotted on the CS-A-MS (Diopside-Anorthite-Enstatite) diagram (Fig. S.5a). Isobaric cotectics are be calculated from:

$$A\ (\text{Anorthite}) = 20.188 - 5.2595P + 0{\cdot}27P^2 + 0{\cdot}5389CS \quad \text{(Herzberg, 2011)}$$

Which yields a pressure of melting in GPa. Equilibrium olivine is then incrementally (0.5% increments) added back into the lava composition until the composition reaches the equivalent pressure cotectic in the Ol-CaTs-Qz projection (Fig. S.5b).

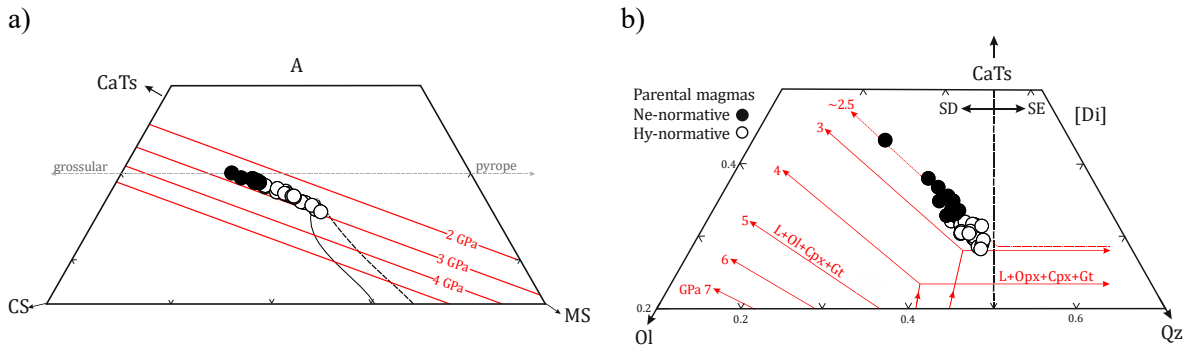

Fig. S.5 a) Molecular projection from or towards olivine onto the plane CS–MS–A (diopside–enstatite–anorthite) for Seal Nunataks parental pyroxenite-derived magmas (black dots). This projection is a larger portion of the garnet-pyroxene plane shown in b), and because the projection is from or towards olivine, olivine fractionation has no effect on the position of individual data points. The black curve separates olivine (to the left) and quartz (to the right) pyroxenite and the pecked curve represents the thermal divide at magma generation pressures, such that magmas to the right and left of the divide have divergent fractionation histories. b) Molecular projection from or toward diopside onto the plane olivine–calcium Tschermak's molecule–quartz for Seal Nunataks parental pyroxenite-derived magmas divided by CIPW normative characteristics (black dots *Ne*-normative; white dots *Hy*-normative). Parental compositions were calculated by adding equilibrium olivine to lavas that are related to the olivine liquidus until they reach the cotectic for the pressure indicated by their position in the projection in a), that is between 2.5 and 3.0 GPa. The vertical pecked line separates silica-deficient and silica-enriched (SD and SE, respectively) at 1 atm.

References cited

Herzberg, C., 2011. Identification of source lithology in the Hawaiian and Canary Islands: implications for origins. J Petrol. 52, 113-146.

Herzberg, C., O'Hara, M.J. 2002. Plume-associated ultramafic magmas of Phanerozoic age. J. Petrol. 43, 1857-1883.

Herzberg, C., Asimow, P.D., 2015. PRIMELT3 MEGA.XLSM software for primary magma calculation: Peridotite primary magma MgO contents from the liquidus to the solidus. Geochem. Geophys. Geosys. 16, 563-578.

Hole, M.J., 2021, Antarctic Peninsula: petrology. Chapter 4.1b. From: Smellie, J. L., Panter, K. S. and Geyer, A. (eds) Volcanism in Antarctica: 200 million years of Subduction, Rifting and Continental Break-up: Geological Society, London, Memoirs, 55. https://doi.org/10.1144/M55-2018-40.

Hole, M.J. & Millett J.M. 2016. Controls of mantle potential temperature and lithospheric thickness on magmatism in the North Atlantic Igneous Province: Journal of Petrology, 57, 417-436. DOI: 10.1093/petrology/egw014

Lambart, S. 2017. No direct contribution of recycled crust in Icelandic basalts. Geochem. Persp. Lett. 4, 7-12. doi: 10.7185/geochemlet.1728

Lambart. S., Baker, M.B., Stopler, E.M., 2016. The role of pyroxenite in basalt genesis: Melt-PX, a melting parameterization for mantle pyroxenites between 0.9 and 5 GPa. J. Geophys. Res. doi: 10.1002/2015JB012762.

Le Roux, V., Dasgupta, R. & Lee, C-T. A. 2015. Recommended mineral-melt partition coefficients for FRTEs (Cu), Ga, and Ge during mantle melting. American Mineralogist, 100, 2533-2544.

McKenzie, D.P., O'Nions, R.K., 1995. The source region of Ocean Island basalts. J. Petrol., 36, 133-159.

Pertermann, M., Hirschmann M.M., Hametner, D., Günther, D., Schmidt, M.W., 2004. Experimental determination of trace element partitioning between garnet and silica-rich liquid during anhydrous. Geochem. Geophys. Geosys., 5. doi:10.1029/2003GC000638

Sun, S-S. & Mcdonough, W. F. 1989. Chemical and isotopic systematics of oceanic basalts: implications for mantle composition and processes. In: Saunders, A.D. & Norry, M.J., (eds). Magmatism in the ocean basins. Geological of Society, London, Special Publications, 42, 313-345.

Tables S1

Peridotite. Mineral modes

	Ol	Cpx	Opx	Gt	Sp
Gt peridotite	0.598	0.076	0.211	0.115	
Modal Gt peridotite	0.12	0.7	0.12	0.06	
Modal spinel peridotite	0.15	0.77	0.06		0.02
Spinel peridotite	0.578	0.112	0.29		0.02

Starting composition and partition coefficients.

Starting Composition		Ol	Cpx	Opx	Gt	Sp
Cs	0.00033	0.0098	0.031	0.022	0.042	0
Rb	0.0333	0.0098	0.031	0.022	0.042	0
Ba	0.4667	0.0099	0.026	0.013	0.023	0
Th	0.0067	0.01	0.03	0.01	0	0
U	0.0020	0.002	0.04	0.01	0	0
Nb	0.0800	0.01	0.005	0.00800	0.01211	0
Ta	0.0053	0.01	0.005	0.00800	0.01211	0
La	0.1200	0.007	0.056	0.002	0.004	0.001
Ce	0.4000	0.0005	0.092	0.02	0.007	0.001
Pr	0.0800	0.01	0.16	0	0	0.01
Sr	6.5	0.014	0.0654	0.06	0.012	0
P	35.0	0.0066	0.11	0.03	0.026	0.01
Nd	0.50	0.001	0.21	0.0068	0.087	0.001
Zr	4.50	0.012	0.1	0.01	0.32	0
Hf	0.122	0.012	0.1	0.03	0.32	0
Sm	0.180	0.0013	0.26	0.01	0.217	0.001
Eu	0.070	0.0016	0.31	0.013	0.32	0.01
Ti	0.090	0.006	0.18	0.016	0.28	0.15
Gd	0.250	0.0015	0.30	0.016	0.498	0.001
Tb	0.047	0.0015	0.31	0.019	0.75	0.001
Dy	0.320	0.0017	0.33	0.022	1.06	0.001
Ho	0.070	0.0016	0.31	0.026	1.53	0.001
Y	2.000	0.01	0.30	0.005	2	0
Er	0.200	0.0015	0.30	0.03	2	0.001
Tm	0.031	0.0015	0.29	0.04	3	0.001
Yb	0.207	0.0015	0.28	0.049	4.03	0.01
Lu	0.031	0.0015	0.28	0.06	5.5	0.01
Ni	1953	6.2	3.2	3.7		10
Zn	55	1	0.48	0.68	0.213	5.2
Mn	1200	1	1.11	0.75	1.24	0.46
Pb	0.0127	0.002	0.0400	0.0100	0.0000	0.0000
Sc	20	0.2	0.8	0.5	6.0	0.1
Co	87	2.1	1.06	1.04	0.83	3

Table S.2

Pyroxenite. Mineral modes

	Ol	Plag	Cpx	Opx	Gt
Gt pyroxenite	0.00	0.00	0.75	0.00	0.25
Modal gt pyroxenite	0.00	0.00	0.75	0.00	0.25
Gt-free pyroxenite	0.00	0.10	0.70	0.20	0.00
Modal Gt-free pyroxenite	0.00	0.10	0.70	0.20	0.00

Starting composition and partition coefficients.

Starting Composition		Ol	Plag	Cpx	Opx	Gt
Cs	0.002	0.0098	0.071	0.002	0.022	0.00825
Rb	0.200	0.0098	0.07	0.002	0.022	0.00825
Ba	2.50	0.0099	0.260	0.0025	0.013	0.005
Th	0.06	0.0100	0.005	0.005	0.010	0.00411
U	0.03	0.0020	0.005	0.0065	0.010	0.018
Nb	1.40	0.0100	0.005	0.0080	0.008	0.01211
Ta	0.09	0.0100	0.005	0.0080	0.008	0.01211
La	1.50	0.0067	0.14	0.0285	0.020	0.0043
Ce	4.50	0.0060	0.111	0.0580	0.040	0.0106
Pr	0.75	0.0005	0.20	0.10	0.050	0.03
Sr	60	0.0140	1.000	0.1500	0.002	0.01325
P	275	0.0066	0.09	0.1345	0.030	0.17333
Nd	4.00	0.0066	0.09	0.150	0.030	0.14
Zr	35	0.0120	0.048	0.1630	0.010	0.55
Hf	1.00	0.0120	0.048	0.245	0.010	0.4474
Sm	1.40	0.0066	0.072	0.2515	0.010	0.36
Eu	0.56	0.0068	0.700	0.30	0.013	0.50
Ti	0.70	0.0060	0.050	0.382	0.100	0.28
Gd	2.10	0.0015	0.066	0.402	0.016	0.90
Tb	0.39	0.0015	0.060	0.400	0.030	1.40
Dy	2.75	0.0096	0.063	0.542	0.019	2.00
Ho	0.63	0.0016	0.048	0.650	0.03	3.00
Y	19.0	0.0100	0.030	0.700	0.03	4.00
Er	1.90	0.0015	0.041	0.6835	0.03	5.23
Tm	0.30	0.0015	0.045	0.720	0.04	7.00
Yb	2.00	0.0140	0.056	0.769	0.04	9.00
Lu	0.30	0.0160	0.053	0.8275	0.06	10.6
Ni	2868	7.00		22.00		8.00
Zn	65	0.980		0.680	0.45	0.89
Mn	1750	0.900		1.60	0.64	4.600
Pb	0	0.002	0.0100	0.04	0.010	0.00
Sc	42	0.2		1.9	0.5	8.0
Co	70	0		0.5	0.8	0.8

Supplementary Information – Analytical techniques

1. Analysis of major and minor elements in olivine by Electron Probe Micro Analyser

The analysis of major and minor elements (Fe, Cr, Si, Ca, Ti, Mn, Al, Mg and Ni) in Seal Nunataks olivines was undertaken using a Cameca SX100 microprobe, fitted with five wavelength dispersive spectrometers, in the Dept of Earth Sciences, University of Cambridge over two days in November 2021. A total of 55 olivine crystals were identified across 10 sections (100 microns thick) made from the Seal Nunataks samples. The selected olivines were typically >1.5 mm and cut down their C-axis to allow for analysis of crystal cores. For easy identification of the chosen crystals during the EPMA, a laser spot was fired into the centre of each olivine crystal (30 μm diameter, 4 J/cm^2 laser fluence, 10 Hz repetition rate, IVA shutter). The EPMA was made around this spot, which also subsequently allowed Laser-Ablation Inductively-Coupled Mass-Spectrometer (see below) analyses on the same spot. Between three and five separate analyses were made on each olivine crystal, except for one especially large Seal Nunataks olivine crystal where ten analyses were carried out. Column conditions were 20 KeV and 40 nA. The secondary standards showed accuracy values (mean values compared to published values) of 100.01% for SiO_2, 99.70% for MgO and 94.52% for FeO. Analytical precision (relative standard deviation, relative to the mean) was 0.27% for SiO_2, 0.43% for MgO and 0.67% for FeO.

The olivines exhibit slight normal zonation in Fo content. The highest Fo of each sample plots within or below the K_D = 0.27 – 0.33 and so are in equilibrium with the melt (Figure 1).

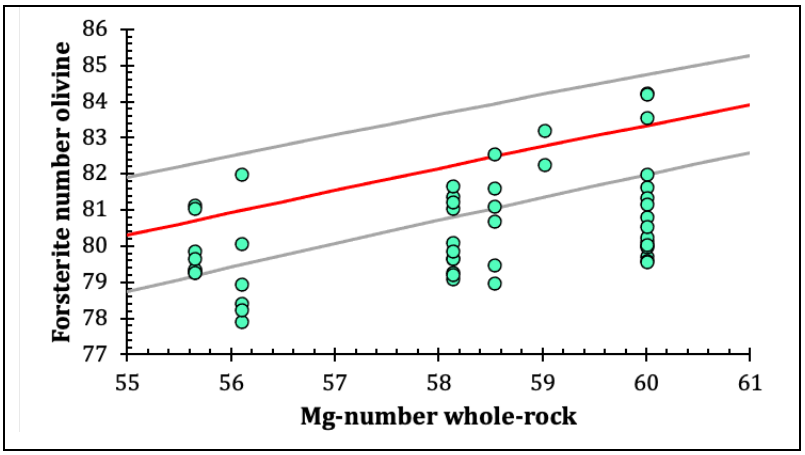

Figure 1: Plot showing the Mg-number of the whole-rock samples plotted against the forsterite number of the constituent olivine crystals from the corresponding Seal Nunataks sample. Whole-rock data are from Hole (1990).

2. Analysis of minor elements in olivine by Laser-Ablation Inductively-Coupled Mass-Spectrometer

The analysis of minor elements in olivine (Li, B, Na, Al, P, Ca, Sc, Ti, V, Cr, Mn, Co, Ni, Cu, Zn, Ga, Y, Zr, Nb, Sn and Pb) was carried out using an ESI NWR193 Laser coupled to a Perkin Elmer Nexion 350D quadrupole-based ICP-MS in the Dept of Earth Sciences, University of Cambridge over two days in November 2021. The instrument was set up with a mass flow control of 600 ml/min and a laser power of 4 J/cm^2 for the duration of the experiment. Laser ablation was carried out on the same spots as EPMA. Three separate analyses were made on each crystal, aside from one especially large Seal Nunatak olivine crystal where six analyses were taken. The diameter of the laser analysis spots varied from 100 μm to 50 μm due to the differing sizes of the olivine crystals and the varying amounts of clean crystal face for contaminant-free analysis. A laser diameter of 100 μm was the default based on findings from Bussweiler *et al*. (2019), who showed that fractionation effects in high-Mg olivines are especially problematic in laser analyses < 75 μm. Figure 6 shows 100 μm laser spots in an olivine crystal. The standards used during the analysis were NIST614, NIST612, NIST610, BHVO-2G, BIR-1G together with in-house standards BD4074 (olivine 3) and 06SGOL3.

The raw data was first calibrated using the NIST612 GeoReM preferred value for SiO_2. The SiO_2 data from the EPMA was also used to calibrate for each individual olivine crystal. The raw data was then processed using peak selection to exclude anomalous signals and background data from the final values. Accuracy was assessed based on the difference between the mean of the analyses of a reference material and the recommended values.

Accuracy (%)	NIST614	NIST612	NIST610	BHVO-2G	BIR-1G
Na23	103.78	100.33	102.69	76.06	81.25
Al27	102.06	100.42	100.43	105.17	102.91
Ca44	100.06	100.32	102.35	96.08	94.33
Sc45		100.39	104.60	96.04	95.77
Ti47	102.95	100.25	112.32	106.46	111.08
V51	97.39	100.19	101.56	106.78	102.58
Cr53	106.72	100.33	103.25	99.52	101.69
Mn55		100.35	98.29	93.13	85.78
Co59	94.94	100.20	103.71	105.45	106.80
Ni60	95.91	100.24	100.74	105.29	101.71
Cu65	129.44	100.19	102.68	99.39	106.62
Zn66	89.61	101.57	108.14	133.25	119.36
Ga69	91.76	100.47	101.55	103.18	103.86

There is good accuracy for the elements used in the analysis. Zn values range from 89.6% to 133.3%, and Mn values range from 85.8% to 102.1%. However, this includes standards with Zn and Mn concentrations that are an order of magnitude smaller than the olivine concentrations. These standards have lower accuracy than would be true for the studied olivine crystals, partially due to the increased effect of natural variation in the sample composition with lower concentrations. Analytical precision was assessed using the relative standard deviation to the mean value (RSD) for standards analysed during the same run as the Seal Nunataks samples (Table 2):

$$RSD = \frac{\sigma}{\mu}$$

Where σ is the sample standard deviation and μ the sample mean

Table 2: Mean RSD values for standards run during the Seal Nunataks LA-ICP-MS session in November 2021.

Mean RSD Values	NIST614	NIST612	NIST610	BHVO-2G	BIR-1G
Na23	0.34	3.17	2.63	5.49	6.63
Al27	7.04	6.56	3.99	3.98	5.14
Ca44	1.48	2.82	2.25	2.55	3.90
Sc45	2.10	3.77	3.00	3.94	3.99
Ti47	12.43	5.21	2.65	3.01	4.06
V51	3.20	2.64	2.01	2.92	4.39
Cr53	N/A	4.63	2.15	3.08	3.59
Mn55	N/A	8.04	2.29	2.75	4.10
Co59	1.33	3.56	2.12	3.76	4.62
Ni60	12.73	3.91	2.17	2.72	3.09
Cu65	4.16	2.92	2.04	5.25	4.29
Zn66	7.41	8.08	2.48	5.72	5.37
Ga69	6.98	4.01	2.21	4.78	3.94

3. Whole-rock analysis by ICP-MS

Samples of Seal Nunatak basalts were analysed for trace and rare earth elements on a Perkin Elmer Nexion 350D quadrupole-based ICP-MS in the Dept of Earth Sciences, University of Cambridge. Each powder was

weighed into a PFA vial to ~ 0.1 g and then digested using hydrofluoric acid and nitric acid. The digested powders were then diluted using deionised water to 50 ml. The samples then underwent a 1/10 dilution into vials (0.300 ml of sample with 2.700 ml of diluting acid) before being analysed. A calibration blank, two procedural blanks, BCR-2, BHVO-2 and AGV-2 were also analysed.

Table 3: Accuracy (mean analytical value*100/published value) of standards run during the ICP-MS session in December 2021.

	BHVO-2	BHVO-2 MM	BHVO-2 MM	BHVO-2	BHVO-2	BHVO-2	Mean	Reference value	% Accuracy
Li	4.39	4.58	5.13	4.80	4.41	4.39	4.62	4.50	103
P	1150	1184	1201	1166	1078	1054	1139	1172	97
K	4026	4369	4179	4130	3912	3802	4070	4258	96
Sc	36.30	38.04	38.47	36.83	33.71	33.17	36.09	31.83	113
Ti	15707	16569	17266	16002	14999	14788	15888	16370	97
V	314.20	317.95	337.99	306.52	296.46	293.13	311.04	318.20	98
Cr	262	282	289	261	263	246	267	287	93
Mn	1246	1323	1380	1286	1295	1261	1298	1309	99
Co	41.56	43.97	45.22	42.93	41.22	40.15	42.51	44.89	95
Ni	106	111	115	110	101	107	108	120	91
Cu	134	141	140	135	129	122	134	129	103
Zn	100.2	108.7	115.6	105.9	97.2	99.7	104.6	103.9	100.6
Ga	20.45	21.73	21.56	20.25	19.93	19.04	20.50	21.37	96
Rb	10.10	10.82	10.73	10.22	9.99	9.72	10.26	9.26	111
Sr	373	400	392	362	381	353	377	394	96
Y	25.13	28.88	27.98	25.26	26.01	25.18	26.41	25.91	102
Zr	155	181	176	159	158	158	164	171	96
Nb	17.04	18.48	18.45	17.46	16.72	16.50	17.44	18.10	96
Sn	1.74	2.06	2.11	1.66	1.68	1.71	1.83	1.78	103
Cs	0.09	0.10	0.10	0.09	0.09	0.08	0.09	0.10	92
Ba	134	143	142	133	131	133	136	131	104
La	15.33	16.36	16.39	14.98	15.20	15.11	15.56	15.20	102
Ce	37.22	39.63	40.18	36.55	36.60	37.15	37.89	37.53	101
Pr	5.31	5.56	5.64	5.13	5.19	5.17	5.34	5.34	100
Nd	24.75	26.40	26.36	23.85	24.32	24.12	24.97	24.27	103
Sm	6.04	6.46	6.55	5.98	6.05	6.08	6.19	6.02	103
Eu	2.07	2.20	2.27	2.06	2.08	2.05	2.12	2.04	104
Gd	6.25	6.96	7.00	6.20	6.34	6.35	6.52	6.21	105

Tb	0.96	1.03	1.03	0.95	0.95	0.95	0.98	0.94	104
Dy	5.29	5.70	5.62	5.15	5.19	5.23	5.37	5.28	102
Ho	0.98	1.05	1.06	0.97	0.97	0.97	1.00	0.99	101
Er	2.52	2.66	2.75	2.47	2.48	2.49	2.56	2.51	102
Tm	0.33	0.36	0.36	0.34	0.33	0.33	0.34	0.33	102
Yb	1.92	2.08	2.09	1.89	1.93	1.91	1.97	1.99	99
Lu	0.27	0.29	0.29	0.26	0.26	0.26	0.27	0.28	99
Hf	4.45	4.69	4.75	4.26	4.41	4.32	4.48	4.47	100
Ta	1.16	1.25	1.25	1.14	1.15	1.13	1.18	1.15	102
Tl	0.02	0.02	0.02	0.02	0.02	0.02	0.02	0.02	90
Pb	1.56	2.32	2.33	1.50	1.51	1.51	1.79	1.65	108
Th	1.22	1.27	1.29	1.17	1.19	1.17	1.22	1.22	99
U	0.43	0.45	0.45	0.42	0.42	0.42	0.43	0.41	104

Table 3 (continued)

	BCR-2	BCR-2 MM	BCR-2	BCR-2 MM	BCR-2	BCR-2	Mean	Reference value	% Accuracy
Li	9.51	11.04	9.07	10.36	8.62	8.53	9.52	9.13	104
P	1515	1624	1462	1591	1467	1315	1496	1568	95
K	13731	15269	13731	14707	13473	12645	13926	14726	95
Sc	39.90	43.60	37.81	41.69	37.88	35.65	39.42	33.53	118
Ti	13328	14592	12879	14063	12847	12045	13292	13576	98
V	421.08	459.91	407.66	434.81	408.09	383.19	419.12	417.60	100
Cr	13	18	13	18	14	13	15	16	94
Mn	1478	1572	1453	1669	1522	1461	1526	1523	100
Co	34.82	37.35	33.76	39.58	35.66	33.80	35.83	37.33	96
Ni	11.20	17.75	11.19	17.61	11.42	10.52	13.28	12.57	106
Cu	25.14	29.46	26.31	30.24	25.59	25.81	27.09	19.66	138
Zn	118.3	130.2	116.0	130.7	118.1	112.4	120.9	129.5	93.4
Ga	20.65	22.44	20.32	22.69	20.49	20.25	21.14	22.07	96
Rb	51.89	57.39	51.49	56.12	51.02	49.75	52.95	46.02	115
Sr	309	351	323	336	311	305	323	337	96
Y	35.20	39.91	35.02	37.77	35.14	33.83	36.15	36.07	100
Zr	180	200	172	189	178	166	181	187	97
Nb	11.87	13.32	11.61	13.00	11.48	11.16	12.07	12.44	97
Sn	2.12	2.61	2.09	2.63	2.14	2.11	2.28	2.28	100
Cs	1.06	1.17	1.04	1.15	1.03	1.04	1.08	1.16	93

Ba	691	743	692	778	693	703	717	684	105
La	25.34	27.31	25.53	28.07	25.44	25.29	26.16	25.08	104
Ce	52.55	57.08	53.43	58.42	52.75	52.92	54.53	53.12	103
Pr	6.70	7.26	6.76	7.48	6.69	6.77	6.94	6.83	102
Nd	28.90	31.44	29.02	32.26	29.10	29.37	30.01	28.26	106
Sm	6.70	7.19	6.69	7.49	6.68	6.81	6.93	6.55	106
Eu	1.93	2.10	1.98	2.18	1.93	1.97	2.02	1.99	101
Gd	6.81	7.45	6.96	7.25	6.73	6.86	7.01	6.81	103
Tb	1.08	1.18	1.08	1.19	1.07	1.07	1.11	1.08	103
Dy	6.36	6.92	6.42	6.98	6.32	6.28	6.55	6.42	102
Ho	1.29	1.39	1.33	1.44	1.30	1.32	1.35	1.31	103
Er	3.64	3.90	3.70	4.08	3.68	3.65	3.77	3.67	103
Tm	0.53	0.57	0.53	0.59	0.52	0.53	0.55	0.53	102
Yb	3.29	3.55	3.29	3.65	3.28	3.31	3.40	3.39	100
Lu	0.49	0.54	0.50	0.54	0.49	0.49	0.51	0.50	101
Hf	4.91	5.30	5.00	5.48	4.90	4.98	5.09	4.97	102
Ta	0.76	0.83	0.79	0.88	0.78	0.78	0.80	0.79	102
Tl	0.25	0.28	0.26	0.29	0.26	0.25	0.26	0.27	99
Pb	10.21	13.00	10.32	13.44	10.19	10.24	11.23	10.59	106
Th	5.86	6.36	5.87	6.46	5.82	5.90	6.04	5.83	104
U	1.71	1.84	1.71	1.89	1.69	1.74	1.76	1.68	105

Table 3 (continued)

	AGV-2	AGV-2	Mean	Reference value	% Accuracy
Li	10.25	9.95	10.10	10.80	94
P	1898	1842	1870	2108	89
K	21372	20015	20693	24056	86
Sc	15.68	14.99	15.33	13.11	117
Ti	5617	5298	5457	6300	87
V	107.88	107.15	107.51	118.50	91
Cr	14	13	13	16	83
Mn	716	701	708	778	91
Co	14.73	13.73	14.23	15.46	92
Ni	16.79	16.15	16.47	18.87	87
Cu	48.21	47.43	47.82	51.51	93
Zn	71.7	74.0	72.8	86.7	84
Ga	19.09	18.81	18.95	20.42	93
Rb	72.63	73.88	73.26	67.79	108
Sr	629	675	652	660	99
Y	19.29	19.99	19.64	19.14	103
Zr	214	226	220	232	95
Nb	12.89	12.68	12.79	14.12	91
Sn	1.83	1.84	1.83	1.83	100
Cs	1.06	1.08	1.07	1.17	91
Ba	1139	1150	1144	1134	101
La	38.20	37.87	38.03	38.21	100
Ce	68.44	68.43	68.44	69.43	99
Pr	7.97	7.97	7.97	8.17	98
Nd	30.57	30.32	30.45	30.49	100
Sm	5.51	5.53	5.52	5.51	100
Eu	1.45	1.43	1.44	1.55	93
Gd	4.24	4.18	4.21	4.68	90
Tb	0.64	0.63	0.64	0.65	98
Dy	3.42	3.44	3.43	3.55	97
Ho	0.67	0.67	0.67	0.68	98
Er	1.80	1.81	1.80	1.83	99
Tm	0.26	0.26	0.26	0.26	99
Yb	1.60	1.61	1.60	1.65	97
Lu	0.24	0.24	0.24	0.25	96

Hf	5.20	5.23	5.21	5.14	101
Ta	0.85	0.83	0.84	0.87	97
Tl	0.26	0.26	0.26	0.28	96
Pb	13.48	13.41	13.44	13.14	102
Th	6.08	6.02	6.05	6.17	98
U	1.91	1.91	1.91	1.89	101

Table 4: RSD values for reference materials run during the ICP-MS session in December 2021.

RSD Values	BCR-2	BHVO-2	AGV-2
Li	9.01	6.51	0.20
P	4.95	3.22	0.18
K	5.21	3.50	2.71
Sc	5.63	4.71	1.28
Ti	5.34	5.16	2.24
V	4.49	4.71	1.42
Cr	14.49	5.51	1.17
Mn	6.00	4.63	0.43
Co	6.52	4.10	3.08
Ni	24.81	4.11	0.82
Cu	8.21	4.11	0.74
Zn	5.59	6.16	3.93
Ga	5.22	4.14	0.86
Rb	5.01	3.70	3.09
Sr	5.01	4.72	6.87
Y	5.14	6.26	4.40
Zr	5.15	6.71	5.63
Nb	6.28	4.34	0.70

Rh	3.17	2.54	1.89
In	1.28	1.76	2.22
Sn	10.85	9.71	1.84
Cs	4.95	5.85	0.91
Ba	5.29	4.32	0.64
La	5.05	4.48	1.89
Ce	5.10	4.57	1.28
Pr	5.26	4.37	1.31
Nd	5.19	4.86	1.85
Sm	5.14	4.29	1.02
Eu	5.44	4.69	2.21
Gd	5.94	5.33	1.96
Tb	5.46	4.54	2.30
Dy	5.41	4.78	0.81
Ho	4.64	4.67	1.02
Er	4.95	4.73	0.85
Tm	5.21	4.63	2.13
Yb	5.19	4.92	0.86
Lu	5.50	4.87	0.95
Hf	4.97	4.67	0.88
Ta	5.77	4.93	2.79
Tl	5.80	5.18	1.84
Pb	14.12	22.83	1.61
Th	5.17	4.56	1.99
U	5.04	3.99	1.39

References

Bussweiler, Y., Giuliani, A., Greig, A., Kjarsgaard, B. A., Petts, D., Jackson, S. E., Barrett, N., Luo, Y. & Pearson, D. G. (2019). Trace element analysis of high-Mg olivine by LA-ICP-MS – Characterization of natural olivine standards for matrix-matched calibration and application to mantle peridotites. *Chemical Geology* **524**, 136–157.

Hole, M. J. (1990). Geochemical evolution of Pliocene-Recent post-subduction alkalic basalts from Seal Nunataks, Antarctic Peninsula. *Journal of Volcanology and Geothermal Research* **40**, 149–167.